Applied Catalysis B: Environment and Energy 353 (2024) 124062

Contents lists available at ScienceDirect

Applied Catalysis B: Environment and Energy

journal homepage: www.elsevier.com/locate/apcatb

Ternary Zn-Ce-Ag catalysts for selective and stable electrochemical CO_2 reduction at large-scale

Ilias Stamatelos [a,b,*], Fabian Scheepers [a], Joachim Pasel [a], Cao-Thang Dinh [c,**], Detlef Stolten [d,e]

[a] Forschungszentrum Jülich GmbH, Institute of Energy and Climate Research, Electrochemical Process Engineering (IEK-14), Jülich 52425, Germany
[b] Faculty of Mechanical Engineering, RWTH Aachen University, Aachen 52056, Germany
[c] Department of Chemical Engineering, Queen's University, Kingston, Ontario K7L 3N6, Canada
[d] Forschungszentrum Jülich GmbH, Institute of Energy and Climate Research, Techno-economic Systems Analysis (IEK-3), Jülich 52425, Germany
[e] Faculty of Mechanical Engineering, RWTH Aachen University, Chair for Fuel Cells, Aachen 52056, Germany

ARTICLE INFO

Keywords:
Zinc oxide
Cerium oxide
Ternary catalysts
Heterostructures
Membrane electrode assembly
Electrochemical CO_2 reduction
CO_2-to-CO
Stability
Large-scale

ABSTRACT

Catalyst materials with high stability and selectivity, based on inexpensive materials, are vital for practical electrochemical carbon dioxide (CO_2) reduction (ECR). In this study, we report ternary Zn-Ce-Ag catalysts for selective and stable CO_2-to-CO conversion at high current densities on a large scale. We found that ZnO catalysts are relatively selective for CO_2-to-CO conversion, but are only stable for less than 20 h at current densities over 100 mA cm^{-2} due to the reduction of the Zn oxide phase, along with the ECR. Combining ZnO with CeO_2 significantly improves the stability of the catalysts, maintaining a CO Faradaic efficiency (FE_{CO}) of 80 % for 100 h at the current density of 200 mA cm^{-2}. By introducing a small amount of silver (<10 wt%) to form ternary Ag-Ce-Zn catalysts, both CO selectivity and stability are significantly improved: the developed catalysts exhibit a high FE_{CO} of 90 % at 200 mA cm^{-2} and are stable for 200 h. We attribute the enhanced CO_2-to-CO conversion efficiency to the abundance of stable interfacial areas of various metal-oxide interactions, which are critical for ECR. To demonstrate the potential for practical application, we performed the ECR in a large electrochemical cell, with an active surface area of 100 cm^2. The system delivers a FE_{CO} of 90 % at 200 mA cm^{-2} for an extended operation time of 200 h.

1. Introduction

The electrocatalytic carbon dioxide (CO_2) reduction reaction (ECR), powered by renewable energy sources, is an emerging process for the viable and sustainable conversion of greenhouse gas CO_2 into value-added chemicals [1–3]. Over the last decade, important progress has been made regarding the fundamental understanding of the ECR [4–6] and its potential applications [7,8]. ECR can produce many different chemicals, depending on the catalyst used [5,9]. Techno-economic assessments have suggested that carbon monoxide (CO) and formate ($HCOO^-$) are products that have the highest economic value, in comparison with other C_{2+} chemicals [10,11]. CO is also an important industrial intermediate for producing various chemicals, including methanol and synthetic fuels [12,13].

CO_2-to-CO conversion is often catalyzed by expensive noble metals, including Ag and Au [14–16]. For practical application, it is essential to develop efficient catalysts from inexpensive and Earth-abundant materials. Transition metal oxide materials, such as zinc oxide (ZnO), have emerged as promising ECR catalysts [17,18]. High CO selectivity (FE_{CO} over 80 %) has been demonstrated in ZnO-based catalysts and those at relatively high current densities of over 100 mA cm^{-2} [19,20]. However, ZnO-based catalysts often suffer from low stability due to depletion of the active ZnO phase during ECR, especially at high current densities [21,22]. As a result, long-term stability (>100 h) at high reaction rates of CO_2-to-CO conversion using ZnO-based catalysts has rarely been demonstrated.

Engineering metal/metal-oxide heterostructures [23] is a promising strategy for developing ECR catalysts with high selectivity and stability [24–26]. The ECR is primarily facilitated by the diverse interfacial active sites within the heterostructures, coupled with their large surface area

* Corresponding author at: Forschungszentrum Jülich GmbH, Institute of Energy and Climate Research, Electrochemical Process Engineering (IEK-14), Jülich 52425, Germany.
** Corresponding author.
E-mail addresses: i.stamatelos@fz-juelich.de (I. Stamatelos), caothang.dinh@queensu.ca (C.-T. Dinh).

https://doi.org/10.1016/j.apcatb.2024.124062
Received 25 September 2023; Received in revised form 30 March 2024; Accepted 8 April 2024
Available online 9 April 2024

[27,28]. Cerium oxide (CeO_2), has attracted a lot of research interest as an active catalyst-supporting material, with applications for the ECR [29–31]. CeO_2 actively contributes to the ECR by enhancing CO_2 adsorption [32], a major step for the overall ECR process [33,34]. CeO_2-based ECR catalysts can be used for the formation of a wide range of products, depending on their constitution [35,36]. The role of the CeO_2-phase was initially demonstrated by Hong et al [37]. using a copper-cerium oxide (Cu-CeO_2) catalyst. They demonstrated that the Cu/CeO_2 interface stabilizes the Cu^{+1} state during the ECR, promoting C_{2+} selectivity [38]. Zong et al [39]. further studied the role of the CeO_2-phase in a zinc-cerium oxide (ZnO/CeO_2) catalyst. The strong Zn-O-Ce interactions stabilized the Zn^{+2} oxidation state during ECR. The ZnO/CeO_2 catalyst recorded a maximum partial current density for the CO (j_{CO}) of -150 mA cm^{-2} with nonetheless limited stability. Fabrication of silver–metal oxide (Ag-MO) interfaces is known to promote CO_2–to–CO conversion [40]. Bhalothia et al [41]. synthesized a ZnO/Ag catalyst of high CO selectivity. The Ag–ZnO heterostructure promotes high ECR activity [42]. The function of the Ag–MO heterostructure was highlighted by Fu et al [43]. Using a Cr_2O_3/Ag catalyst, they recorded high FE_{CO} (90 %) and prolonged ECR stability ($>$ 25 h). The CO_2–to–CO turnover was promoted over the Ag–Cr_2O_3 interphase. During ECR, the Cr_2O_3 substrate maintained the Cr^{+3} state, eliminating structural degradation and favoring prolonged ECR.

In this work, we developed selective and stable Zn-Ce-Ag oxide catalysts for the CO_2-to-CO conversion. Exploiting the ECR-active ZnO and Ag phases, we sought to increase the CO selectivity. The stable CeO_2-phase aided in stabilizing the oxidation state of Zn^{+2} and moderating the agglomeration rate of the ZnO- and Ag-phase. Our materials were evaluated directly in a membrane electrode assembly (MEA) electrolyzer, allowing us to operate at high current densities. Initially, we optimized the structure and composition of the ZnO-CeO_2 catalyst, which exhibited a CO Faradaic Efficiency (FE_{CO}) of 80 % at 200 mA cm^{-2} for 100 h. By adorning this material with a low amount (5 %) of silver (Ag), we recorded 90% FE_{CO} at 200 mA cm^{-2} for 200 h of continuous ECR operation. The strong metal-metal/oxide interactions in the composite material were responsible for the catalyst's activity and stability. We exhibited the real application potential of our material by showcasing its performance in a large MEA electrolyzer with a 100 cm^2 active area. We managed to record similarly high performance and stability in the large cell as in the small-scale one.

2. Experimental part

2.1. Materials

We obtained zinc nitrate hexahydrate ($Zn(NO_3)_2{\cdot}6H_2O$, 99.99 %), potassium bicarbonate ($KHCO_3$, 99 %), silver nitrate ($AgNO_3$, 99.99 %), ethanol (anhydrous), cerium (IV) sulfate (anhydrous $Ce(SO_4)_2$, 99.99 %), and sodium perchlorate ($NaClO_4$, 99.999 %) from Sigma-Aldrich without the need for additional purification. We obtained Iridium/iridium (III) oxide nanopowder (IrO_x, nanopowder 99.99 %) and silver nanopowder (99.99 %, 20–40 nm) from Alfa-Aesar without the need for purification or treatment. We obtained demineralized water (MiliQ), carbon paper (Freudenberg H23C6), porous transport layers made from titanium fibers (Ti-PTL, with a thickness of 500 μm), Nafion dispersed in alcohol-based solution at a weight percentage of 5 % wt/wt, and carbon black (Cabot Vulcan XC-72) from the Fuel Cell Store. Additionally, we purchased a Sustainion Membrane of X37–50 grade RT from Dioxide Materials.

2.2. Catalyst preparation

The various catalyst materials were prepared using wet chemical methods and subjected to a final high-temperature calcination step.

ZnO nanoparticles (ZnO-np): A solution of $Zn(NO_3)_2$ with a concentration of 0.2 M was prepared by combining 50 ml of the solution with 50 ml of KOH with a concentration of 0.4 M. The addition of KOH was done drop by drop at a rate of 1 ml per minute while stirring the mixture continuously until the process was complete. The resulting precipitate was separated using centrifugation and then washed three times with water (MilliQ) followed by one wash with ethanol. After that, the product obtained from this process was dried overnight at a temperature of 70 °C and subjected to calcination for three hours at an air temperature set at 500 °C to achieve crystallization and form the crystalline phase composed mainly of ZnO.

CeO_2 nanoparticles (CeO_2-np): A solution of 0.2 M $Ce(SO_4)_2$, with a volume of 50 ml, was prepared in water. Dropwise addition (drop rate of 1 ml min^{-1}) of a 0.5 M KOH solution took place while stirring until the pH reached 9. We collected the precipitant by centrifugation and was sequentially washed three times with MilliQ water and once with ethanol. The end product was later dried overnight at a temperature of 70 °C and subjected to calcination for three hours at 500 °C under an air atmosphere that remained static, leading to the formation of crystalline CeO_2.

cpZnCeX nanoparticles: We prepared a solution consisting of 50 ml of water with the appropriate molar ratios of $Ce(SO_4)_2$ and $Zn(NO_3)_2$. The total amount of precursors remained constant at 0.1 moles. The variable X represents the content of Ce, which we adjusted to 5 %, 10 %, and 20 %. We then added a solution of KOH (0.5 M concentration) drop by drop (at a rate of 1 ml per minute) while stirring, until achieving a pH value of 9. Afterward, we collected the precipitant through centrifugation and washed it three times with MilliQ water and once with ethanol. The end product was later dried overnight at a temperature of 70 °C and subjected to calcination for three hours at 500 °C under an air atmosphere that remained static, leading to the formation of crystalline phases of the material.

csZnCeX nanoparticles: We prepared a 50 ml aqueous solution containing the appropriate amount of core CeO_2-np and $Zn(NO_3)_2$. This solution was then placed in a sonication bath for 60 min to create a uniform dispersion. The total molar amount of the precursors remained constant at 0.1 moles. X represents (%) the concentration of Ce, and we varied this concentration at values of 5, 10, and 20%. To this dispersion, we added a dropwise solution of KOH with a concentration of 0.5 M under stirring conditions until the pH reached between 9 and 10. We collected the precipitate through centrifugation and washed it three times with MilliQ water followed by one wash with ethanol. The end product was later dried overnight at a temperature of 70 °C and subjected to calcination for three hours at 500 °C under an air atmosphere that remained static, leading to the formation of crystalline phases of the material.

Ag@cpZnCe10 nanoparticles: We created a 50 ml solution by combining 100 mg of cpZnCe10 nanoparticles and 40 mg of $AgNO_3$. To optimize the material, we adjusted the amount of $AgNO_3$ precursor to vary the amount of silver. The dispersion was then placed in a sonication bath for one hour to ensure it was evenly distributed. Next, we added dropwise a solution of 0.25 M KOH under stirring conditions until reaching a pH level between 9 and 10. The resulting precipitate was collected through centrifugation and washed three times with water (MilliQ) followed by one wash with ethanol. We then dried the product overnight at 70 °C before calcining it for two hours at 250 °C in a static air atmosphere.

Ag@csZnCe10 nanoparticles: The synthesis of this material followed the same process as outlined above (Ag@cpZnCeX nanoparticles). Instead of the precursor solution, cpZnCeX nanoparticles were used as the core material.

Ag@ZnO**:** In a typical synthesis, 100 mg of ZnO–np and $AgNO_3$ were dispersed in 50 ml of water (60 min sonication bath). In the dispersion, 0.25 M of KOH was added dropwise (1 ml min^{-1}), under stirring conditions, until a pH value of 9–10 was reached. We varied the $AgNO_3$ amount to achieve an Ag-doping of: 5, 10, and 15 %. The sample was gathered using centrifugation and rinsed with water (MilliQ) thrice, followed by a single wash with ethanol. The resulting material was then

dried for an entire night at a temperature of 70 °C before undergoing calcination for 2 h at 250 °C in the presence of stationary air.

2.3. Electrode preparation

All gas diffusion electrodes (GDEs) were made using Freudenberg (H23C6) carbon paper by utilizing an automated spray-coating machine (Sono-Tek, ExactaCoat). To make the ink for the GDEs, 120 mg of catalyst powder, 30 mg of carbon black, 12 ml of isopropanol, 7.5 ml of Milli-Q water, and 158.3 μl of Nafion solution (5 % wt./wt.) were combined. The catalyst inks were then subjected to Ultra-Turex at a speed of 33,000 rpm for ten minutes before being placed in a sonication ice bath for sixty minutes. The same ink formulation (consisting of solids and solvents in specific proportions) was utilized for all other catalyst inks mentioned in this study. The cathode GDEs that contained the catalyst had a loading level of 1 mg cm^{-2}. Following, the GDEs underwent drying at a temperature of 70 °C for three hours. This gentle heat treatment aided in evaporating the remaining surfactants from both the ionomer suspension and solvents used during production.

To conduct electrochemical measurements and assess the performance of MEAs (membrane electrode assemblies), GDEs (gas diffusion electrodes) with a catalyst material loading of 1 mg cm^{-2} were utilized. For the anode of the MEA, a porous transport layer (PTL) made from Ti fiber mesh (Bekaert) was employed. The initial Ti-PTL underwent etching in boiling HCl (1 M), eliminating the outer passivating TiO_x layer. After etching, IrO_x nanoparticles (Alfa-Aesar) were sprayed onto the PTL to fabricate the anode catalyst layer. The ink recipe for the anode catalyst layer was: 160 mg of IrO_x and 800 mg of Nafion ionomer dispersed in a 5 % wt./wt. ethanolic solution, which was then mixed with 60 ml of methanol. This ink mixture underwent Ultra-Turex treatment at 33,000 rpm for 10 min followed by sonication in an ice bath for one hour. The loading amount for pure IrO_x was maintained at 1 mg cm^{-2}.

2.4. Electrochemical measurements

To evaluate the reduction of CO_2 in the MEA configuration, a specially designed cell with a 2 cm^2 (1×2 cm^2) active area was utilized. The anode consisted of IrO_x/Ti–PTL, and the anolyte was 0.1 M $KHCO_3$. A Sustainion AEM (X37–50 RT) membrane with a thickness of 50 microns was employed. Before entering the cell, the CO_2 (30 sccm), is passed through a humidifier at room temperature. The used PTFE gasket had a thickness of 400 μm and the assembly of the cell involved applying three Nm torque to each screw of the electrolyzer. The smaller MEA was held together by four screws, whereas for larger MEAs, eight screws were used for assembly. In both cases, catalyst-loaded GDEs served as cathode materials and were placed facing toward the AEM membrane during assembly. To generate a polarization curve, the cell was operated continuously at a fixed current for 25 min. Throughout this period, the voltage (on average) required to maintain this current was measured and the gas products were sampled after 20 min. Regarding the larger MEAs with an active area of 100 cm^2 (10×10 cm^2), another custom-built cell configuration was employed. The process of assembly remained unchanged, with the cathode, anode, anolyte, and membrane being identical to those utilized in the 2 cm^2 MEA. A PTFE gasket with a thickness of 400 μm was employed (with equal compression for both cells), and 5 Nm of torque was applied during assembly. Before entering the cell, the CO_2 (1500 sccm) underwent humidification at room temperature. To heat the larger cell, heating rods were inserted into its housing successively raising temperatures to 40 °C and then 60 °C. The different electrochemical experiments were conducted using an AUTOLAB potentiostat supported by Nova software as a means of control.

To examine the CO_2 reduction products in the flow cell and MEA reactors, we utilized inline gas chromatography from PerkinElmer. This analysis employed a thermal conductivity detector (TCD) and a flame ionization detector (FID). Argon (99.999 %) was used as the carrier gas. The measurement of the gas flow rate at different points along the polarization curve was conducted at the gas outlet of the cell.

2.5. Mechanical pressure distribution analysis of the MEA

For a single MEA cell, the distribution of the mechanical pressure was determined by pressure-sensitive films that were obtained from Fujifilm Europa (GmbH). The cells were assembled using PTFE foils of the same thickness as those used during the electrochemical experiments. The cells contained the electrode substrates of the anode and cathode, without any catalyst layer. The Fujifilm was placed in between the anode and cathode electrode substrates without adding any AEM. The original data was deconvoluted using the 'FPD-8010E' software.

2.6. Electrochemical characterizations

The flow cell (Electro-Cell) used for the electrochemical experiments had a 1 cm^2 active area, using Ni-foam as an anode. The set-up was used for the Tafel slopes and potentiostatic electrochemical impedance spectroscopy (PEIS) analysis of the GDEs. The electrolyte that was utilized had a concentration of 1 M KOH, with passed at 4.6 ml min^{-1} and the CO_2 passed had a flow rate of 15 sccm. To measure the applied potentials during these experiments, an Ag/AgCl reference electrode was employed. These potentials were then related to an RHE through the following equation: $E_{RHE} = E_{Ag/AgCl} + 0.059\ pH + E_{o,\ Ag/AgCl}$, where $E_{o,\ Ag/AgCl}$ is equal to 0.1976 V. All of these experiments were carried out at room temperature (RT). The evaluation of Tafel slopes focused on the catalysts' kinetic region (-5 to −15 mA cm^{-2}), while PEIS measurements were conducted at the onset potential of each Gas Diffusion Electrode (GDE) within a frequency range of 10^5- $4 \bullet 10^{-2}$ Hz. To assess the electrochemical surface area (ECSA), the double-layer capacitance (C_{dl}) was calculated for each GDE. The catalyst layers had uniform amounts of loading, and their compositions primarily consisted of ZnO at approximately 80 %. By directly comparing C_{dl} values, trends in ECSA could be observed among different GDEs loaded with various catalysts. The experiments took place in an H-cell using an Ag/AgCl reference electrode and a Pt wire as a counter-electrode. A standard electrolyte solution containing 0.1 M $NaClO_4$ was used, which had been saturated with argon gas. Cyclic voltammetry scans were conducted at scan rates ranging from 20 to 100 mV sec^{-1}. Current density measurements were obtained from the non-faradaic region of the cyclic voltammograms.

2.7. Characterization of the catalyst materials

The X-ray diffraction (XRD) analysis was conducted on the crystalline phase of both the original materials and the prepared GDEs. This analysis utilized CuKα radiation with a 2θ range of 25–100 °, using a Shimadzu XRD-6000 diffractometer. To determine the surface compositions of the catalysts, X-ray photoelectron spectroscopy (XPS) was employed. The instrument used for this analysis was the Phi5000 VersaProbeII by ULVAC-Phi Inc., USA, utilizing Al K-alpha radiation at a monochromatic energy of 1.486 keV. The X-ray settings were as follows: 50 W power, 15 kV voltage, and a spot size of 200 μm. For obtaining survey spectra, pass energy of 187.5 eV with an increment step size of 0.8 eV and acquisition time per step set to be at 100 ms/step were applied; whereas for detailed spectra acquisition pass energy changed to be 23.5 eV with an increment step size reduced to be only 0.1 eV while keeping time per step constant at 100 ms. The elemental composition analysis for each catalyst material was performed using inductively coupled plasma optical emission spectroscopy (ICP-OES). To initiate this process, probes were dissolved in dilute nitric acid (HNO_3), followed by their subsequent examination via ICP–OES using the iCAP7600 instrument.

RAMAN spectroscopy provided additional information on the organization and arrangement of the materials. To accomplish this, an iXR Raman Spectrometer from Thermo Fisher Scientific was utilized. The

powder form of the catalysts served as the subject of analysis. The laser used for excitation had a wavelength of 600 nm. To observe the morphology of both catalyst powders and GDEs, a scanning electron microscope (SEM) was employed. Specifically, the Zeiss 1550 VP SEM with a Gemini column was utilized at voltages up to 30 keV. TEM and HRTEM measurements were conducted using a Philips CM 200 field emission gun with an accelerating voltage set at 200 kV. To achieve optimal "Z-contrast" conditions, a probe semi-angle of 25 mrad was employed alongside an inner collection angle of 70 mrad by the detector.

3. Results and discussion

3.1. Development and characterisation of Zn-Ce binary oxides for the ECR

Through our wet-chemical synthesis approach, we successfully synthesized our initial binary Zn-Ce oxide catalyst materials [44]. By employing either co-precipitation or sequential precipitation, we varied the morphology of the catalysts, forming the cpZnCe or the csZnCe respectively [45]. To synthesize our ternary ZnCeAg oxide catalysts, we deposited silver (Ag) over the surface of the Zn-Ce oxides from a precursor Ag^{+} solution [46]. Decorating the surface of the csZnCe and csZnCe oxides precursors with fine Ag-nanoparticles (experimental section, Fig. S1) forms Ag@csZnCe and Ag@cpZnCe ternary oxide catalysts, respectively. The differences in catalyst morphologies and compositions are expected to influence their catalytic properties significantly [47].

High-Resolution Transition Electron Microscopy (HRTEM) was used to characterize the morphology and structure of Zn-Ce oxide catalysts synthesized using the two different synthesis approaches (Fig. 1a-d). With the gradual co-precipitation approach, a composite oxide with two distinct phases of ZnO and CeO_2 was obtained (Fig. 1a, b). The distinct phases in the form of nanoclusters of 5 nm radius were evenly distributed throughout the material's structure (Fig. S5a-d). This mixed-phase structure enabled a large interfacial area between the ZnO and CeO_2 crystal planes. The catalyst synthesized via the sequential precipitation approach results in the architecture of the csZnCe10, with the ZnO being settled around the CeO_2 cores (Fig. 1c, d) and mostly exposed over the catalyst's surface (Fig S2). The material was constituted of CeO_2 nanoparticle cores covered with a thick layer (12 nm) of ZnO (Fig. 1c-d). The HRTEM images (Fig. 1a-d), suggest that the preparation of the different materials was successfully undertaken.

To confirm the crystalline structures of the catalysts, we performed X-ray diffraction (XRD) on the catalyst materials (Fig. 1e). The ZnO phase was identified as having a hexagonal wurtzite structure (PDF No. 01–089–0510), whereas the CeO_2 phase could be indexed into the fluorite-hexagonal structure (PDF No. 34–0394 & 23–1048) [48,49] in both samples, regardless of the synthesis methods used.

The Survey XPS of csZnCe10 and cpZnCe10 (Fig. S2) reveals differences in the surface constitution of each catalyst. The actual elemental composition of all samples was determined using Inductively Coupled Plasma–Optical Emission Spectroscopy (ICP–OES) and can be accurately seen in Table S1. The cpZnCe10 surface exhibits a similar Zn/Ce ratio, with the elemental constitution recorded for the material (Table S1). This feature reveals a uniform phase distribution over the material's core and surface, adopted through the co-precipitation synthesis approach. The Survey-XPS of the csZnCe10 (Fig. S2) reveals a much lower Ce concentration over the catalyst's surface. The different composition of the csZnCe10 surface relates to its structured architecture (adopted through the sequential precipitation approach), majorly exposing the ZnO phase. The comparison of the Zn-XPS (Fig. 1f) of the two samples suggests that Zn remains in the same oxidation state. The Zn–XPS for the cpZnCe10 displays a shifting of 0.7 eV to the Zn–2p3 binding energy (BE) [50]. The close contact of the ZnO and CeO_2 phases, at their interface, induces changes in the local electronic structure of the catalyst [51–54]. These interfacial interactions are mainly present in the cpZnCe10 material, owing to its architecture (Fig. 1a, b). The sequential depletion of the electronic density around the Zn atoms is associated with the positive shift in the BE. The O-XPS (Fig. 1g) of the materials displays a clear difference in the nature of the O-bonds over the materials' surfaces. For the cpZnCe10, the O1s-spectra reveals a high concentration of oxygen disorders, ascribed collectively to vacancies and lattice defects (V_o). The O1s-spectra of the csZnCe10 suggests a lower concentration of V_o. The surface bonded-O was mainly spent in the Zn-oxide phase (34.3 %), which was related to the observed structured architecture of the sample (Fig. 1c, d). The positive shift (0.3 eV) of the O-XPS for the cpZnCe10, indicates depletion of the e^{-} density around the O-atoms. This behavior is associated with the strong interfacial interactions between the ZnO and CeO_2 phases, which is favored in the cpZnCe10 morphology [55,56]. The Ce–XPS (Fig. 1h) indicates that Ce exists in the Ce^{+3} and Ce^{+4} states at different concentrations for each sample. The Ce–XPS of the cpZnCe10 records higher Ce^{+3} concentrations (21.3 %) than in the csZnCe10, which correlates with the increased V_o observed in the cpZnCe10 (Fig. 1g). The absence of a binding energy shift implies that the Ce atoms experience a similar coordination environment, for the different architectures. Suggesting that the interactions between the ZnO and CeO_2 phases primarily affect the Zn and O species, leading to detectable shifts in their XPS signals (Fig. 1f, g). While the Ce atoms remain relatively unaffected. owning to the Ce redox stability [57, 58]. The differences in the coordination environment and electronic state of the surface atoms are majorly attributed to the different architectures of the materials, promoting synergistic interactions among the ZnO and CeO_2 phases [32,39,59].

We evaluated the electrocatalytic activity of the prepared samples for the ECR using a MEA cell. To test the performance of the catalysts in a zero-gap cell set-up, we formed the MEA using catalyst-coated GDEs, an anion exchange membrane, and an IrO_x/Ti felt as the anode. First, we sought to study the effect of the Ce amount on the ECR performance in both catalyst structures. In the cp samples (Fig. S3), increasing the amount of Ce led to an increase in the reaction overpotential (η) and a decrease in the FE for CO (FE_{CO}) (Fig. S3a–c). Among the cp samples, cpZnCe10-GDE exhibited the highest partial current density for CO (j_{CO}, 140 mA cm^{-2}) (Fig. S3d). A similar trend was observed in cs samples, with csZnCe10-GDE exhibiting the highest performance (Fig. S4a–c) recording 150 mA cm^{-2} of j_{CO} (Fig. S4d). The effect of catalyst structure on the ECR performance is summarized in Fig. 2a–d. The introduction of Ce resulted in a partial reduction of the FE_{CO} in comparison to the ZnO-GDE (Fig. 2a–c). The csZnCe10-GDE records higher j_{CO} (150 mA cm^{-2}) and lower overpotential (Fig. 2d). The primary ECR-active phase in the binary oxide catalysts, is predominantly ZnO [60]. The structured architecture adopted by the csZnCe10 catalyst with high ZnO surface exposure exhibits higher ECR activity and j_{CO}.

To investigate the effect of the introduction of Ce on the stability of ZnO-based catalysts, we applied a constant current density of 200 mA cm^{-2} to the MEA electrolyzer and monitored the changes in the products over time. The ZnO–GDE was stable for less than 10 h at a current density of 200 mA cm^{-2} (Fig. 2e), as a result of the reduction of the ZnO phase to metallic Zn [44]. The introduction of Ce greatly improves the stability of the catalyst, effectively prolonging the ECR's lifetime in comparison to the pure ZnO–GDE (Fig. 2e). CeO_2 in composite materials is known to stabilize the oxidation state of the surrounding phases [61,62]. The CeO_2 in our catalysts stabilizes the Zn^{+} state, which is the ECR active one, during electrolysis, prolonging the composite catalyst's stability [63]. While the chemical stability of the CeO_2 allows it to withhold its structure during ECR. The morphology of the cpZnCe10 favors high contact among the ZnO and CeO_2 phases. In addition, the ZnO at the ZnO/CeO_2 interface in cpZnCe10 is accessible and serves as the active phase for ECR. In contrast, due to the structured architecture, most of the ZnO at the ZnO/CeO_2 of csZnCe10 is not accessible for ECR. In this csZnCe10, only external ZnO domains, which are far from the ZnO/CeO_2 interface, are active for ECR. As a result, the

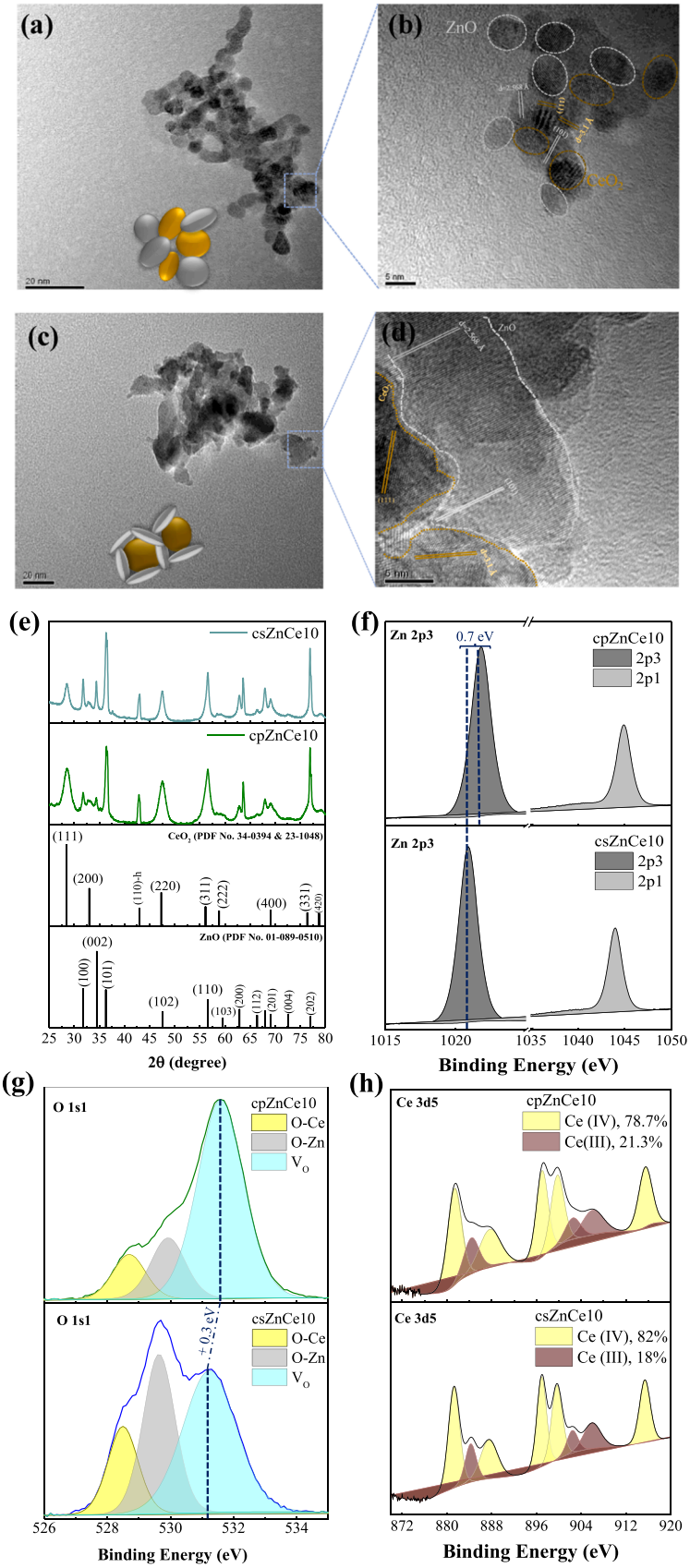

Fig. 1. Structural and physicochemical characterization of the Zn–Ce oxide catalyst powders. (a, b) HRTEM images of the cpZnCe10 catalyst powder; (c, d) HRTEM images of the csZnCe10 catalyst powder; (e) XRD diffractograms of the catalyst materials; (f) high-resolution zinc (Zn2p3) XPS of the catalysts; (g) high-resolution oxygen (O1s1) XPS of the catalysts; (h) high-resolution cerium (Ce3d5) XPS of the catalysts.

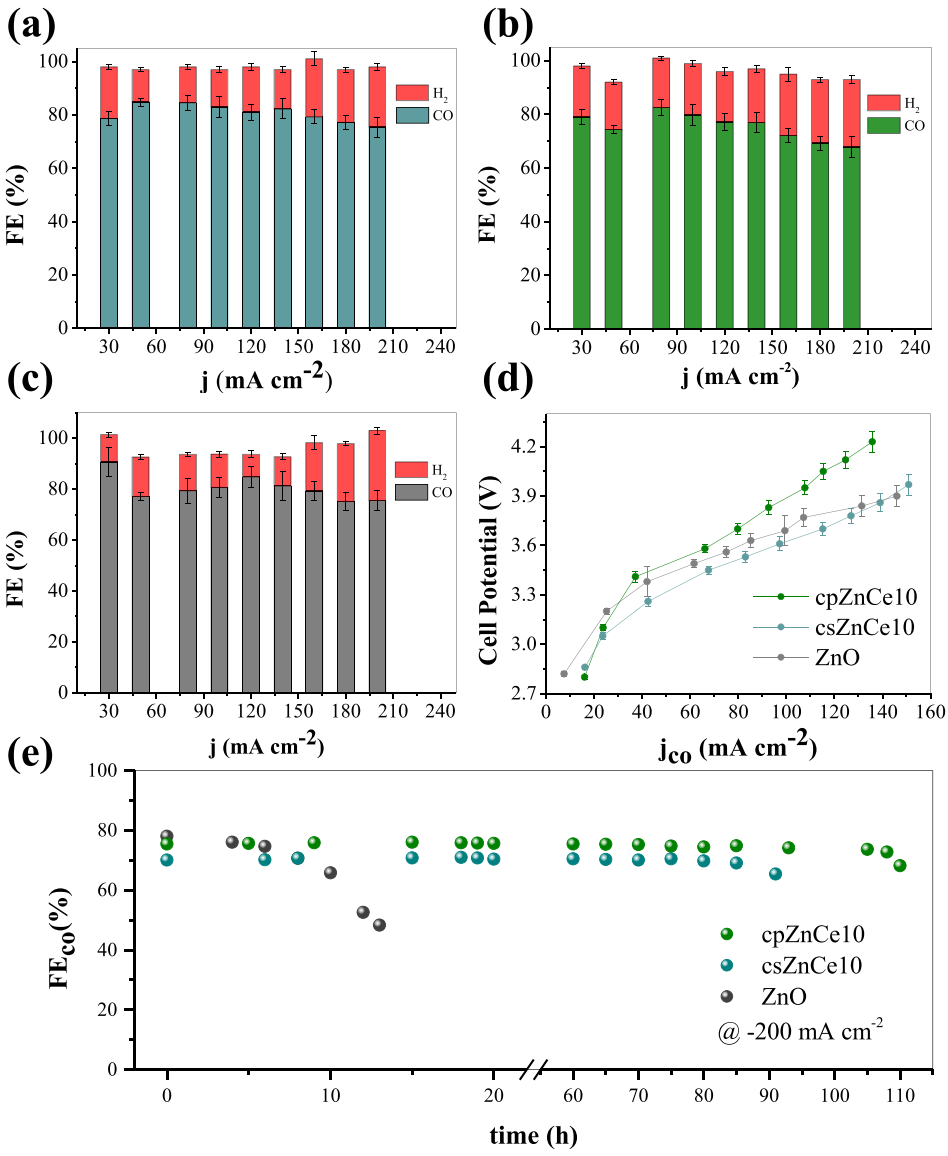

Fig. 2. ECR performance in the MEA of the Zn–Ce oxide catalyst-loaded GDEs and of the baseline ZnO–GDE. (a) Selectivity (FE_{CO}) of the csZnCe10; (b) selectivity (FE_{CO}) of the cpZnCe10; (c) selectivity (FE_{CO}) of the ZnO; (d) polarization curves for the partial current density for CO (j_{CO}), of the various GDEs; (e) stability of the catalyst-loaded GDEs in the MEA system at 200 mA cm^{-2}.

cpZnCe10-GDE maintained a stable FE_{CO} of over 70 % for more than 90 h, while the csZnCe10 was stable for only 80 h. Following the long-term ECR, the GDEs were analyzed using Scanning-Electron-Microscopy (SEM) and HRTEM. The long-term ECR was halted for the csZnCe10-GDE at 85 h and for the cpZnCe10-GDE at 105 h (when the FE_{CO} dropped below 70 %). Both the cpZnCe10 and csZnCe10 GDES form agglomerates (50 nm) comprising mainly from small CeO_2 particles (10 nm) and the Zn/ZnO phase (Fig. S6c–f). Potassium carbonate salts are also a reason for the GDE's degradation (Fig. S6a, b) and are derived from the anolyte (0.1 M $KHCO_3$). The salt formation relates to the potassium ions' (K^+) crossover, through the AEM, towards the cathode GDE. The SEM and HRTEM (Fig. S6g–h) of the post-mortem csZnCe10-GDEs (csZnCe10_LT–GDE) reveals that the catalyst was severely agglomerated, forming large agglomerates of ~100 nm. The post-mortem XRD analysis of the cpZnCe10 and csZnCe10 GDEs (Fig. S6i), revealed that the ECR-active ZnO phase was mostly maintained after the long-term ECR which could result from the stabilizing effect of CeO_2. The architecture appears to have a direct impact on the stability of the GDEs. The partial reduction of ZnO to Zn-metallic led to agglomerations over the GDE. Despite the changes in the ZnO phase, the CeO_2 remained chemically and morphologically stable (Fig. S6b). The architecture of csZnCe10 reduces the contact and interactions between the ZnO and CeO_2 phases (Fig. 2f, g). In the csZnCe10, the predominant ECR activity comes from the external ZnO, located away from the interface. The ZnO phase exhibits behavior similar to a conventional ZnO catalyst. Consequently, this configuration contributes to the ease of destabilizing the Zn oxidation state.

3.2. Development and characterization of Zn–Ce–Ag ternary oxides for the ECR

The results presented above suggest that adding Cerium oxide can stabilize ZnO catalysts for ECR, but that this also decreases CO selectivity. To improve CO selectivity, we doped Zn–Ce catalysts with Silver (Ag), which is known for its selective CO formation, and has also been used for that purpose in various metal/metal-oxide catalysts [24,43,64]. To form Ag NPs over the Zn–Ce surface, we employed an additional precipitation step (Experimental Section). The Ag introduced into the cpZnCe10 and csZnCe10 samples resulted in the Ag@cpZnCe10 and Ag@csZnCe10 samples, respectively.

The XRD diffractograms of the Ag@cpZnCe10 and Ag@csZnCe10 samples (Fig. 3a) reveal that the ZnO phase remains coordinated in the wurtzite system (PDF No. 01–089–0510). The CeO_2 is indexed into the fluorite-hexagonal structure (PDF No. 34–0394 & 23–1048), as observed for the cpZnCe10 and csZnCe10 samples (Fig. 1e). The Ag introduced is in its metallic form, coordinated in the face-centered cubic (FCC) system (PDF No. 04–0783). The HRTEM images of the Ag@cpZnCe10 catalyst (Fig. 3b–d) confirm the presence of Ag NPs smaller in size than 5 nm. The Ag@cpZnCe10 morphology induces the contact of the phases in the ternary oxide. Fig. 3e represents the final morphology of the Ag@cpZnCe10, as observed from the HRTEM (Fig. 3b–d). This architecture favors the contact of the Zn and Ce phases (core of the material) with the Ag phase (shell of the material).

Raman spectroscopy was employed to provide more details regarding the metal/metal-oxide interactions in the catalyst materials. The Raman spectra (Fig. 3f) of all of the samples reveal the main characteristic peaks of the Zn–O (wurtzite-structured ZnO) [65], with a distinct peak even in the ternary oxide samples [41]. The broadening of the Zn–O peak in ternary oxides is attributed to interactions with Ag–O, which has Raman peaks at similar wavenumbers [71,72]. The CeO_2

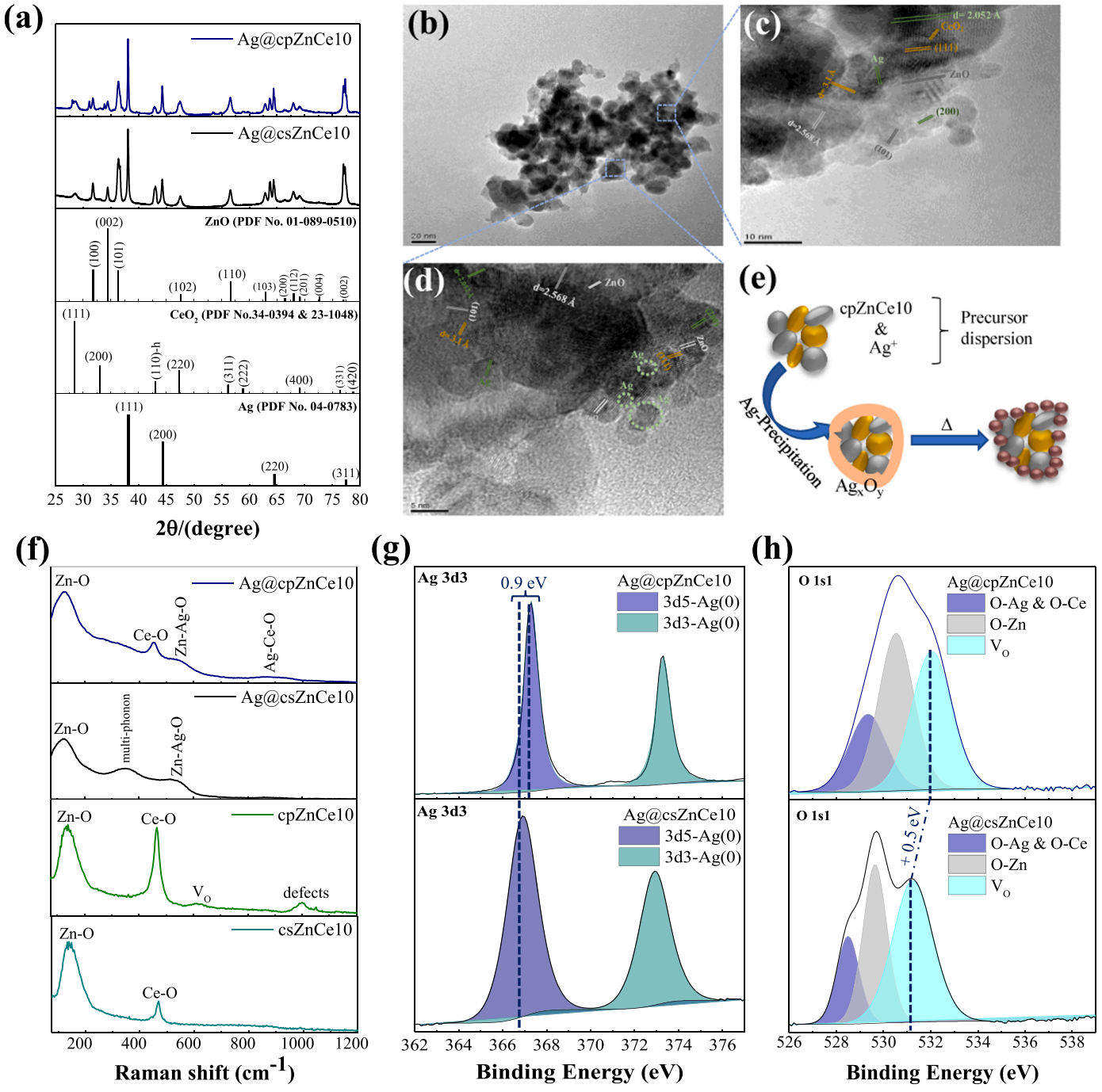

Fig. 3. Structural and physicochemical characterization of the Zn–Ce–Ag oxide catalyst powders. (a) XRD diffractograms of the different catalyst powders; (b–d) HRTEM images of the Ag@cpZnCe10 catalyst powder; (e) graphical illustration of the synthesis route for the Ag@cpZnCe10 catalyst; (f) Raman spectra for both the ternary and Zn–Ce oxide catalyst powders; (g) high-resolution oxygen (O1s1) XPS of the Ag@cpZnCe10 and Ag@csZnCe10 catalysts; (h) high-resolution silver (Ag3d3) XPS of the Ag@cpZnCe10 and Ag@csZnCe10 catalysts.

phase exhibits distinct excitation peaks, attributed to the Ce–O (fluorite structure) vibrations. However, in the Ag@csZncs10 sample, the fluorite excitation peak is attenuated due to the broad multi-phonon Raman peak. The Raman spectra of the cpZnCe10 sample exhibited additional excitation peaks, corresponding to a high concentration of V_o and lattice defects in the material (650 and 1090 cm^{-1}, respectively) [66–70]. The spectra of the Ag@csZnCe10 and Ag@cpZnCe10 samples indicate strong Zn–Ag–O [73–75] interactions in both materials. The Ag@cpZnCe10 spectrum records an additional peak (D_2 at 900 cm^{-1}) ascribed to Ag–Ce–O interactions, revealing a high contact area across all of its phases [46,76–80].

The high-resolution Ag-XPS (Fig. 3g) exhibits a positive shift of 0.9 eV in the Ag-3d5 binding energy (BE) attributed to the Ag@cpZnCe10 catalyst. This behavior suggests strong Ag–O (Fig. 3h) between Ag and oxygen atoms from the ZnO-CeO_2 matrix. The Ag–Ce–O Raman interactions (Fig. 3h) also contribute further to the shifting of the BE. These interactions could involve the formation of bonds of similar nature or surface coordination complexes, shifting the charge density around the Ag-atoms [81]. The high-resolution O-XPS of the materials (Fig. 3h) reveals higher concentrations of V_o than in the Ag@csZnCe10 spectra. This behavior agrees with the high concentration of V_o observed in the Raman spectra of the Ag@cpZnCe10 and the cpZnCe10 matrix (Fig. 3f). The positive shift of the O-XPS signal for the Ag@cpZnCe10 is consistent with the shift observed for the O-XPS of the cpZnCe10 matrix (Fig. 1g). The concentration of V_o in the Ag@cpZnCe10 is lower than that in its precursor cpZnCe10 catalysts. This trend is attributed to the effect of the synthesis condition during the incorporation of Ag. The additional heat treatment required to form the final ternary oxide (2.2), resulted in a lower V_o concentration. The observed shift in the O-XPS is linked to distinct phase interactions within the ternary oxide. After Ag incorporation, additional Ag-O, Ag-Ce-O, and Zn-Ag-O interactions emerge (Fig. 3f), influencing the oxidation state and electron distribution of oxygen atoms which lead to a larger shift (0.5 eV) of the O-XPS for the Ag@cpZnCe10 (Fig. 3h).

Based on the results presented above, we chose cpZnCe10-GDE, which exhibits the highest stability, as the starting material for optimizing the amount of Ag loading in the range of 5–30 wt%. The addition of Ag over the initial catalyst material drastically increases the FE_{CO}

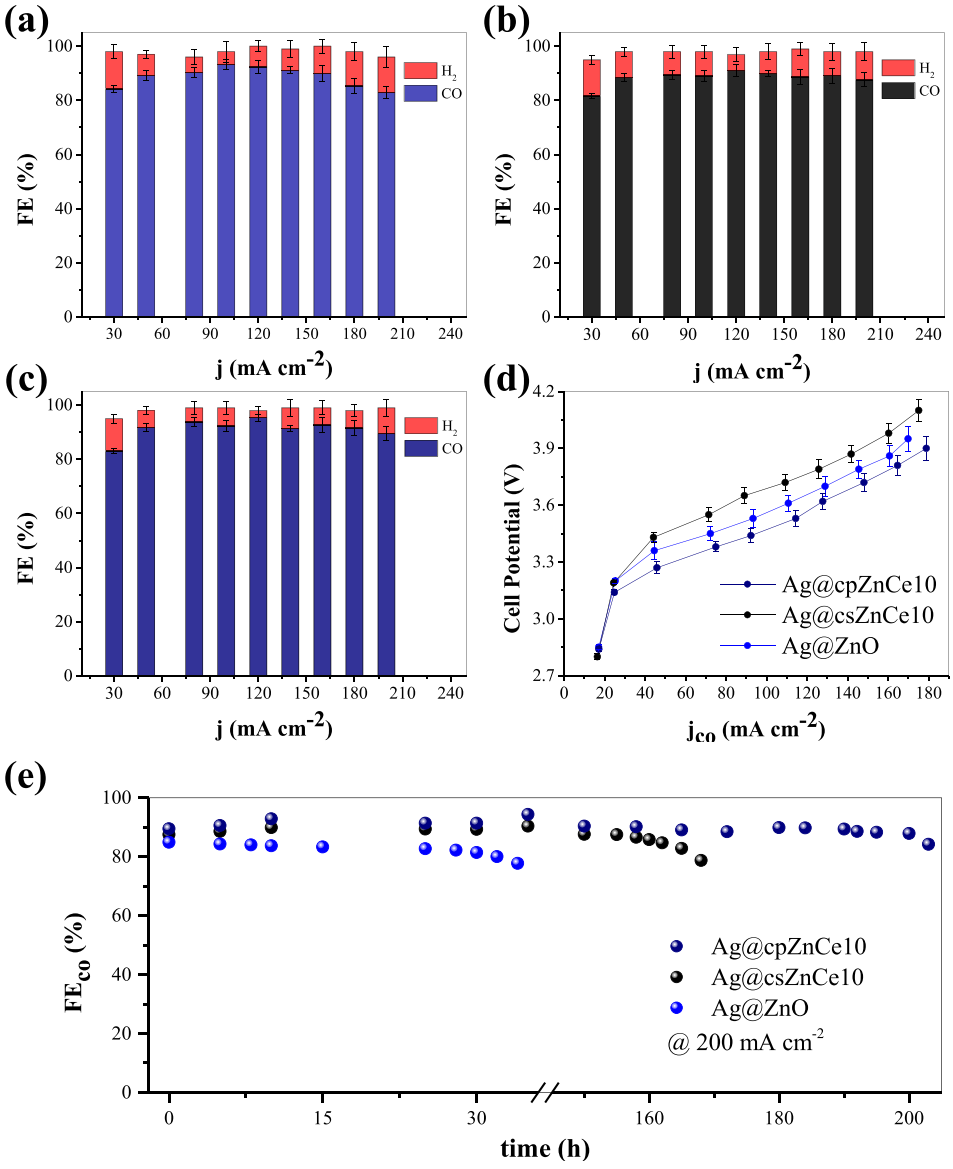

Fig. 4. ECR performance in the MEA electrolyzer of the Zn–Ce–Ag oxide catalyst-loaded GDEs and of the baseline Ag@ZnO-GDE. (a) Selectivity (FE_{CO}) of the Ag@cpZnCe10; (b) selectivity (FE_{CO}) of the Ag@csZnCe10; (c) selectivity (FE_{CO}) of the Ag@ZnO; (d) polarization curves for the partial current density for CO (j_{CO}), of the various GDEs; (e) stability of the different GDEs in the MEA system, at 200 mA cm^{-2}.

(Fig. S8). The variation of the Ag content does not significantly affect the FE_{CO} of the GDEs. On the other hand, Ag loading was found to affect the cell voltage, as shown in the polarization curves (Fig. S8e). A sample with 5 wt% Ag loading shows the lowest overpotential (η) and reaches the highest j_{CO}. The potentiostatic electrochemical impedance spectroscopy (PEIS) of these samples (Fig. S9a) reveals that a 5 wt% of Ag (sample Ag@ZnCe10) exhibits the lowest charge transfer resistance (R_{ct}). A higher Ag content increases the catalyst's R_{ct} by inhibiting the electrocatalytic functions of the created metal/metal–oxide interfaces of the material (Fig. 3c,f) [43,82]. For comparison, we also performed the ECR test using the Ag@csZnCe10 sample derived from the csZnCe10 catalyst covered with Ag (5 wt%). The PEIS of our catalyst materials (Fig. S9b) illustrates that the function of the metal/metal–oxide interfaces and the presence of Ag actively improves the R_{ct} of the materials, especially that of the Ag@cpZnCe10.

Upon the introduction of Ag over the initial catalyst materials (cpZnCe10, csZnCe10, and ZnO), there is a significant improvement in the FE_{CO} (Fig. 4a–c). The catalyst-loaded GDEs reach an FE_{CO} of 90 % at a high current density of 200 mA cm^{-2}. The polarization curves (Fig. 4d) indicate that the catalyst materials reach a high j_{CO} of above 150 mA cm^{-2}. The Ag@cpZnCe10-GDE reaches the highest j_{CO} (180 mA cm^{-2}), introducing at the same time the lowest overpotential for the CO_2-to-CO conversion. The stability of the ternary oxide catalysts (Fig. 4e) was drastically improved after the introduction of Ag. Both the Ag@cpZnCe10 and Ag@csZnCe10 exhibit drastically improved ECR stability. The Ag@cpZnCe10-GDE recorded the longest ECR stability, of 200 h at 200 mA cm^{-2}, maintaining 90 % FE_{CO}. The improved ECR performance of the Ag@cpZnCe10 compared to its cpZnCe10 precursor could be attributed to the effect of Ag in the ternary oxide. The Ag-nanoparticles, formed in the ternary oxide, provide additional active sites, promoting the ECR activity. The Ag@cpZnCe10 morphology favors the formation of additional Zn-Ag-O and Ce-Ag-O interactions (Fig. 3f) which provide additional ECR active sites, making the Ag@cpZnCe10 the most active catalyst from our ternary oxides.

The measured PEIS of the catalyst-loaded GDEs (Fig. S9b) reveals differences in the charge transfer resistance (R_{ct}) introduced by each catalyst. The Ag@cpZnCe10-GDE introduces the lower R_{ct} (5.2 Ω), implying a lower ECR overpotential. The material's ECSA (Fig. S9c) indicates that the Ag-containing samples exhibit higher surface areas than the Ce–Zn oxide counterparts. The Ag@cpZnCe10 has the highest C_{dl} (hence ECSA), implying higher concentrations of catalytically active sites. The Tafel slope analysis of the catalyst-loaded GDEs (Fig. S9d) suggests that the Ag@cpZnCe10 exhibits the fastest kinetics for the CO (-42 mV/dec) and the highest exchange current density (4.73 mA cm^{-2}). The Ag@csZnCe10 exhibits lower ECR kinetics than the Ag@csZnCe10, with a slope of −46 mV/dec and R_{ct} of 10.1 Ω. These results indicate that the morphology of the Ag@cpZnCe10 favors the creation of additional Ag-ZnO and Ag-Ce-O interactions (Fig. 3f), as opposed to the Ag@csZnCe10, further enhancing the performance of the Ag@cpZnCe10. Both the cpZnCe10 and csZnCe10 precursors exhibit

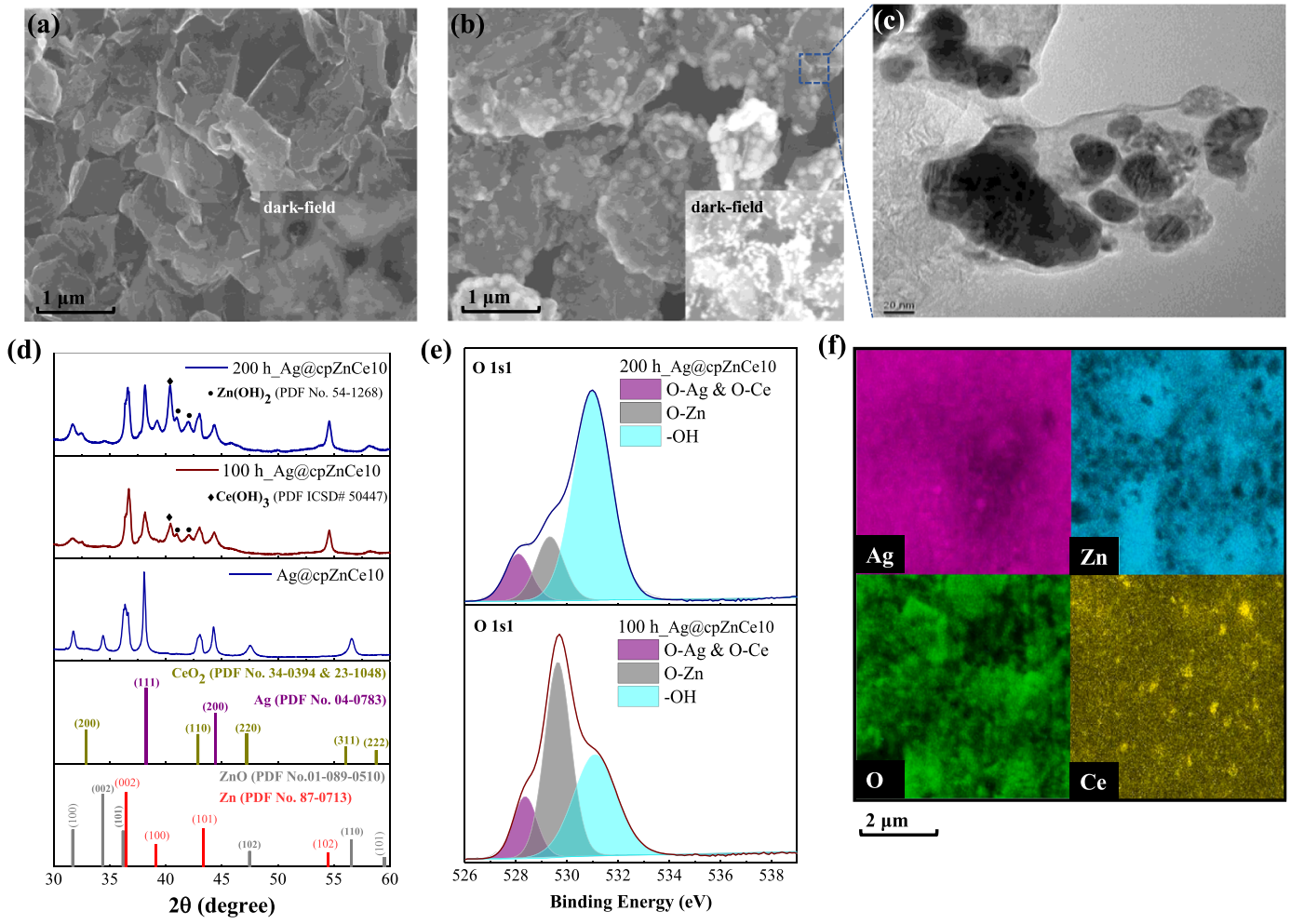

Fig. 5. Post-mortem characterization of the Ag@cpZnCe10–GDE at different times, after ECR at 200 mA cm^{-2} in an MEA electrolyzer. (a) SEM/dark-field-SEM after 100 h of ECR; (b) SEM/dark-field-SEM after 200 h of ECR; (c) HRTEM image of the catalyst after 200 h of ECR; (d) XRD-diffractograms of the catalyst-loaded GDEs after 200 h and 100 h of ECR; (e) high-resolution O-XPS after 200 h and 100 h of ECR; (f) EDX images of the Ag@cpZnCe10–GDE after 200 h of ECR.

lower ECR activity with Tafel-Slopes of −57 mV/dec and −51 mV/dec respectively, and R_{ct} of 22.3 Ω and 18.4 Ω respectively. The faster Tafel kinetics and reduced R_{ct} of the ternary oxide catalysts (Fig. 4d, e), support their higher ECR activity (Fig. 2d, e), as a result of the Ag-addition.

The increased Ag@cpZnCe10 ECR stability compelled us to understand the structural changes of the catalysts during the ECR reaction. We characterized the catalysts before and after the stability test. Initially, the Ag@cpZnCe10 exhibited a uniform elemental distribution (Fig. S11d), owing to the small particle size comprising each of the catalyst's phases (Fig. 3d). After 100 h of ECR, the Ag@cpZnCe10 adopts an altered morphology (Fig. 5a). Dark-field SEM (DF-SEM) can only differentiate between Ce and Zn/Ag due to their large difference in atomic weights. The DF-SEM reveals that the CeO_2 phase begins separating from the initially homogeneous ternary oxide structure (Fig. S11c, d). Through the ECR, the Ag and ZnO phases merge into nano-plate structures, whereas the CeO_2 phase coordinates smaller, separated nano-particles. After 200 h of ECR electrolysis, the CeO_2 phase separation becomes more evident, with the CeO_2 agglomerates increasing in size (Fig. 5b, c). The ECR-active ZnO–Ag phase retains a nano-plate structure after 200 h of ECR. The XRD diffractograms of the Ag@cpZnCe10 GDEs after 200 h of ECR (Fig. 5d) indicate the formation of metallic Zn, $Zn(OH)_2$, and $Ce(OH)_3$. These phase transitions are correlated with the altered morphology adopted by the Ag@cpZnCe10 (Fig. 5a–c). The post-ECR high-resolution O1s1-XPS of the Ag@cpZnCe10 (Fig. 5e) shows that surface oxygen is increasingly spent in bonds of a hydroxide nature. The concentration of the O–Ce and O–Ag surface bonds remains constant, confirming that the Ag and CeO_2 phases retain their stability during the ECR. To investigate the changes that occur in the CeO_2 phase, we examined the effect of 100 h ECR, at 200 mA cm^{-2}, on a CeO_2–GDE. The physicochemical changes of the CeO_2 were isolated on the partial Ce^{+4}-to-Ce^{+3} reduction (Fig. S12a&b), which took place (as a non-Faradaic process) alongside the ECR [83,84]. These changes are associated with the CeO_2 phase being coordinated in fine nano-particle structures (Fig. S11e, f). The CeO_2 phase underwent the same structural changes in both the Ag@cpZnCe10–GDE and CeO_2–GDE during the ECR.

Despite the Ag@cpZnCe10 and Ag@csZnCe10 catalysts having the same composition, their different architectures appeared to affect their ECR stability (Fig. 4e) significantly. The long-term stability of the Ag@cpZnCe10–GDE indicates that its architecture favors ECR stability. The Ag@csZnCe10 morphology changes in a different aspect during long-term ECR. The initially structured architecture, coordinates the Ag–ZnO agglomerates (after 160 h of ECR), covering the CeO_2 cores (Fig. S11g, h). The co-precipitation synthesis approach of the Ag@cpZnCe10 induces the uniform distribution of the phases, promoting the role of the CeO_2 in stabilizing the ECR-active ZnO–Ag phase. It can therefore be illustrated that the ECR-inert CeO_2 assumes the role of a spacer in the composite Ag@cpZnCe10 catalyst. In this respect, the CeO_2 nano-particles withhold the aggregation of the ECR-active ZnO–Ag phase. Observing the *post-mortem* characterization of the Ag@ZnO GDE (Fig. S11i, j) after 30 h of ECR, we can see the formation of large agglomerates. The absence of CeO_2 led to the quick aggregation of the ZnO and Ag phases. It becomes clear that the prolonged stability of the Ag@cpZnCe10 is not only based on the CeO_2 stabilizing the ZnO oxidation state through the ECR (Fig. 5d) but also on the function of the CeO_2 nanoparticles as spacers, procrastinating agglomerates formation. The stability of the CeO_2 phase and associated interactions (Fig. 3f) are attributed to the long-term stability of the Ag@cpZnCe10 catalyst [81].

The Ag@cpZnCe10 GDE exhibits much longer stability than its cpZnCe10 precursor. As previously discussed, the degradation progress is similar for both materials. In the Ag@cpZnCe10, the additional Ag-metallic and the resulting ZnO-Ag & Ag-Ce-O sites provide additional ECR-active sites. These additional phases enhance the ECR during long-time operation, mitigating the effect of the degradation process. Prolonged ECR leads to phase migration (Fig. 5a–c), making the role of CeO_2 as a spacer become less effective. The ZnO–Ag ECR-active phase becomes agglomerated, whereas the formation of $Zn/Zn(OH)_2$ (Fig. 5d) further undermines the ECR activity of the Ag@cpZnCe10 GDE.

3.3. Integration of the developed ECR catalyst in a 100 cm^2 MEA electrolyzer

Electrolysis at elevated temperatures (60–80 °C) is widely adopted in various electrochemical systems, including PEM, AEM, and Fuel Cells. This practice aims to expedite the reaction kinetics and lower overall cell potential, effectively reducing the energy requirements of the electrochemical process. This renders the process more feasible for real-world industrial applications. For these reasons, we sought to evaluate the performance of our ECR-catalysts at higher temperatures. We performed the reaction in a 100 cm^2 electrolyzer to gauge their performance under industrially-relevant conditions. At room temperature, we obtained similar performance as in the small MEA in terms of both j_{CO} and FE_{CO} (Fig. 6a). At 40 °C, the FE_{CO} was limited to around 80 %, whereas at 60 °C the selectivity was stabilized at 70 % for CO (Fig. 6b, c). Although lower cell potentials were obtained at higher temperatures, FE_{CO} decreased due to the increase of HER kinetics along with the ECR. At 60 °C, the maximum j_{CO} recorded was 150 mA cm^{-2} at a full-cell potential of 3.2 V (Fig. 6d), significantly lower than the potential recorded at room temperature. The effect of the temperature on the system's overpotential (Fig. S14a) was also evident from the galvanostatic impedance spectroscopy (GEIS) performed. The GEIS of the MEA (Fig. S14b) exhibited a decrease in the system's electrical resistance, following the temperature increase. We performed the ECR (at room temperature) at 200 mA cm^{-2} for 200 h to investigate the stability of the scaled-up system (Fig. 6e). Throughout the electrolysis period, the system maintained a stable FE_{CO} of 90 % and an energy efficiency for CO (EE_{CO}) of 27 %.

The distribution of the mechanical pressure over the active area of the MEA was investigated (Fig. S14d). In the large MEA, both the imprints of the cathode and anode flow-fields were visible, indicating a uniform distribution of mechanical pressure (Fig. S13d), with the pressure in between the cathode's channels being below three MPa. This analysis ensures that no mechanical overpressure was built into the 100 cm^2 active area, which could have been caused by the scaled-up cell architecture. The low pressure in the cathode channels ensured no deformation of the soft carbon paper that could prevent CO_2 delivery to the cathode catalyst layer. The uniform pressure distribution indicates that the anode and cathode electrodes were in contact and electrochemically active in the entire active area of the MEA (Fig. S14b, d). After long-term ECR electrolysis (200 h), the resistance of the MEA was increased (Fig. S14c). This feature is associated with the catalyst's agglomeration and degradation processes (Fig. 5b, c) along with carbonate precipitants on the cathode catalyst layer (Fig. S15a–c), undermining the MEA's ECR activity.

4. Conclusions

We developed a stable and selective catalyst for CO_2-to-CO conversion based on ternary Zn–Ce–Ag components. We found a composite material of Ce– and Zn–oxide could maintain the ZnO phase, leading to a stable CO_2-to-CO conversion at 200 mA cm^{-2} for 100 h. However, the FE_{CO} of the Zn–Ce binary catalysts was relatively low, below 80 % in the tested current range of 100–200 mA cm^{-2}. To improve the CO selectivity of Zn–Ce, we developed Zn–Ce–Ag ternary oxide catalysts that exhibited a stable FE_{CO} of 90 % at 200 mA cm^{-2} for 200 h. The strong interactions between the different phases cooperatively enhanced the ECR performance, while our results suggested that the enhanced stability of the catalyst mainly originated from the contribution of the CeO_2 phase. The redox stability of CeO_2 aided in both maintaining its structure and also stabilizing the ZnO, during ECR. Most importantly, CeO_2 acted as a spacer moderating the agglomeration of the active Zn–O–Ag

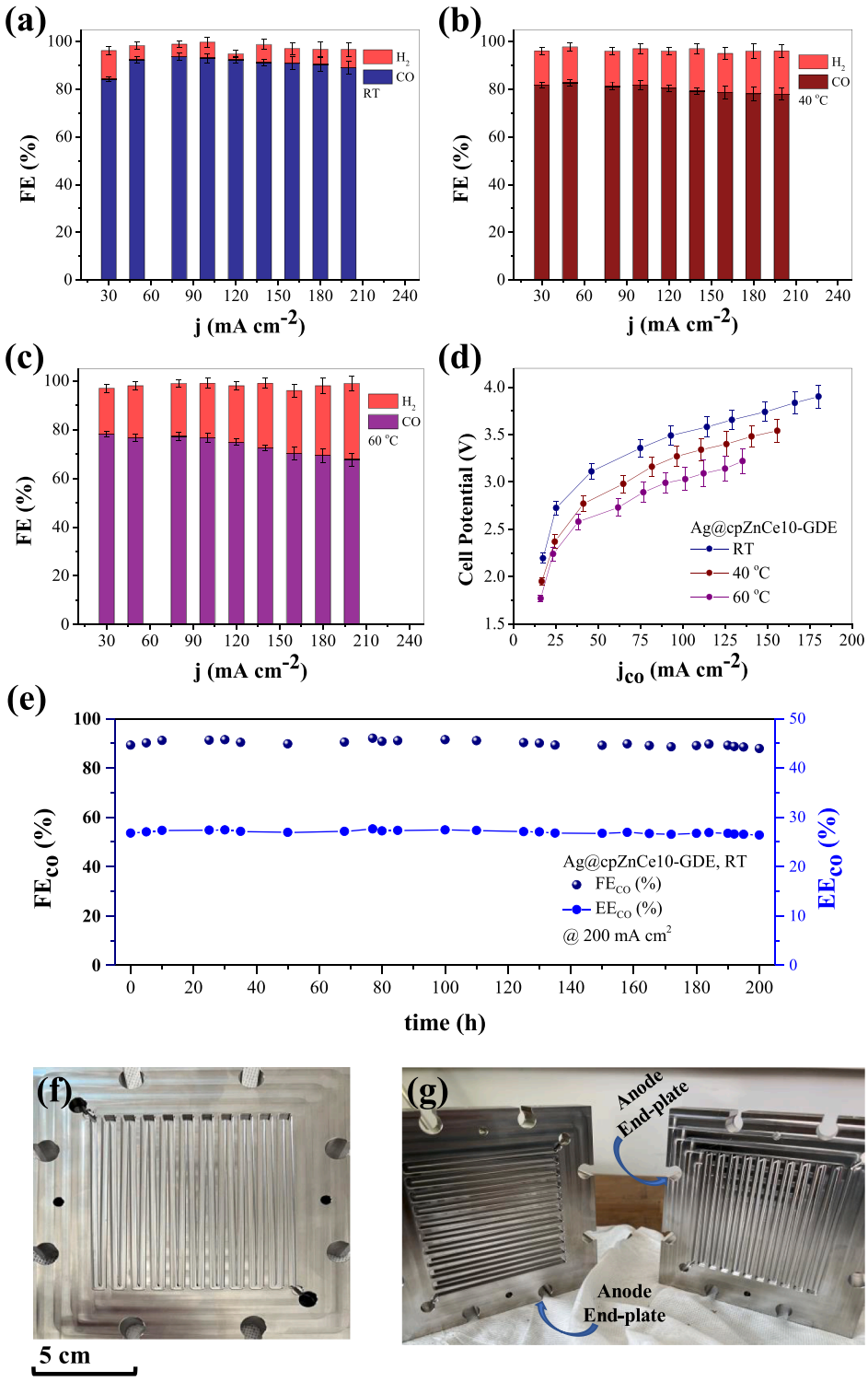

Fig. 6. ECR performance of the Ag@cpZnCe10-GDE in the large MEA (100 cm^2 active area). (a) FE_{CO} of the Ag@cpZnCe10-GDE at room temperature (RT); (b) FE_{CO} of the Ag@cpZnCe10–GDE at 40 °C; (c) FE_{CO} of the Ag@cpZnCe10-GDE at 60 °C; (d) polarization curves for the partial current density for CO (j_{CO}), of the Ag@cpZnCe10-GDE at different temperatures; (e) stability of the Ag@cpZnCe10–GDE, at 200 mA cm^{-2} (at room temperature); (f) image of the flow-field of the 100 cm^2 MEA electrolyzer; (g) image of the two end-plates and current collectors of the 100 cm^2 MEA electrolyzer.

phase, prolonging the catalyst's lifetime. We further demonstrated the potential for the practical application of our Zn–Ce–Ag catalysts by performing ECR using a large MEA electrolyzer with a 100 cm^2 active area. A similar trend was also observed with the large-scale electrolyzer in which the catalysts were not only selective (FE_{CO} of 90 %) but also stable for 200 h at the tested current density of 200 mA cm^{-2}. Our work represents a significant step towards practical CO_2-to-CO conversion utilizing inexpensive catalysts.

CRediT authorship contribution statement

Ilias Stamatelos: Writing – original draft, Validation, Methodology,

Conceptualization. **Cao-Thang Dinh:** Writing – review & editing, Validation, Supervision, Conceptualization. **Joachim Pasel:** Validation. **Fabian Scheepers:** Validation. **Detlef Stolten:** Supervision.

Declaration of Competing Interest

The authors declare that they have no known competing finacial interests or personal relationships that could have appeared to influence the work reported in this paper.

Data availability

Data will be made available on request.

Appendix A. Supporting information

Supplementary data associated with this article can be found in the online version at doi:10.1016/j.apcatb.2024.124062.

References

[1] R. Peters, et al., A techno-economic assessment of Fischer–Tropsch fuels based on syngas from co-electrolysis, Processes (2022), https://doi.org/10.3390/pr10040699.
[2] E.V. Kondratenko, et al., Status and perspectives of CO2 conversion into fuels and chemicals by catalytic, photocatalytic and electrocatalytic processes, Energy Environ. Sci. (2013), https://doi.org/10.1039/C3EE41272E.
[3] O.S. Bushuyev, et al., What should we make with CO2 and how can we make it, Joule (2018), https://doi.org/10.1016/j.joule.2017.09.003.
[4] S. Nitopi, et al., Progress and perspectives of electrochemical CO2 reduction on copper in aqueous electrolyte, Chem. Rev. (2019), https://doi.org/10.1021/acs.chemrev.8b00705.
[5] X. Liu, et al., Understanding trends in electrochemical carbon dioxide reduction rates, Nat. Commun. (2017), https://doi.org/10.1038/ncomms15438.
[6] J. Rosen, et al., Mechanistic insights into the electrochemical reduction of CO2 to CO on nanostructured Ag surfaces, ACS Catal. (2015), https://doi.org/10.1021/acscatal.5b00840.
[7] T. Zheng, et al., Recent advances in electrochemical CO2-to-CO conversion on heterogeneous catalysts, Adv. Mater. (2018), https://doi.org/10.1002/adma.201802066.
[8] F. Liang, et al., Recent development of electrocatalytic CO2 reduction application to energy conversion, Small (2021), https://doi.org/10.1002/smll.202100323.
[9] R. Kortlever, et al., Catalysts and reaction pathways for the electrochemical reduction of carbon dioxide, J. Phys. Chem. Lett. (2015), https://doi.org/10.1021/acs.jpclett.5b01559.
[10] M. Jouny, et al., General techno-economic analysis of CO2 electrolysis systems, Ind. Eng. Chem. Res. (2018), https://doi.org/10.1021/acs.iecr.7b03514.
[11] G.O. Larrazábal, et al., Building blocks for high performance in electrocatalytic CO2 reduction: materials, optimization strategies, and device engineering, J. Phys. Chem. Lett. (2017), https://doi.org/10.1021/acs.jpclett.7b01380.
[12] S. Verma, et al., A gross-margin model for defining technoeconomic benchmarks in the electroreduction of CO2, ChemSusChem (2016), https://doi.org/10.1002/cssc.201600394.
[13] J.M. Spurgeon, B. Kumar, A comparative technoeconomic analysis of pathways for commercial electrochemical CO2 reduction to liquid products, Energy Environ. Sci. (2018), https://doi.org/10.1039/C8EE00097B.
[14] S. Pérez-Rodríguez, et al., Electrochemical behavior of the carbon black Vulcan XC-72R: Influence of the surface chemistry, Int. J. Hydrog. Energy (2018), https://doi.org/10.1016/j.ijhydene.2018.03.040.
[15] C.-T. Dinh, et al., High rate, selective, and stable electroreduction of CO2 to CO in basic and neutral media, ACS Energy Lett. (2018), https://doi.org/10.1021/acsenergylett.8b01734.
[16] Y. Chen, et al., Aqueous CO2 reduction at very low overpotential on oxide-derived Au nanoparticles, J. Am. Chem. Soc. (2012), https://doi.org/10.1021/ja309317u.
[17] A. Stalinraja, et al., Electrochemical reduction of CO2 on Cu doped titanium nanotubes—an insight on ethylene selectivity, Electrochim. Acta (2022), https://doi.org/10.1016/j.electacta.2022.141078.
[18] Q. Xiang, et al., Heterostructure of ZnO nanosheets/Zn with a highly enhanced edge surface for efficient CO2 electrochemical reduction to CO, ACS Appl. Mater. Interfaces (2021), https://doi.org/10.1021/acsami.0c20302.
[19] C. Li, et al., Zn nanosheets coated with a ZnS subnanometer layer for effective and durable CO2 reduction, J. Mater. Chem. A (2019), https://doi.org/10.1039/C8TA10799H.
[20] X. Zong, et al., Morphology-controllable ZnO catalysts enriched with oxygen-vacancies for boosting CO2 electroreduction to CO, J. CO2 Util. (2022), https://doi.org/10.1016/j.jcou.2022.102051.
[21] A.M. Asiri, et al., Revisiting the impact of morphology and oxidation state of Cu on CO2 reduction using electrochemical flow cell, J. Phys. Chem. Lett. (2022), https://doi.org/10.1021/acs.jpclett.1c03957.
[22] M. Ma, et al., Selective and efficient reduction of carbon dioxide to carbon monoxide on oxide-derived nanostructured silver electrocatalysts, Angew. Chem. Int. Ed. (2016), https://doi.org/10.1002/anie.201604654.
[23] X. Feng, et al., Grain-boundary-dependent CO2 electroreduction activity, J. Am. Chem. Soc. (2015), https://doi.org/10.1021/ja5130513.
[24] G.O. Larrazábal, et al., Synergistic effects in silver–indium electrocatalysts for carbon dioxide reduction, J. Catal. (2016), https://doi.org/10.1016/j.jcat.2015.12.014.
[25] H. Xie, et al., Boosting tunable syngas formation via electrochemical CO2 reduction on Cu/In2O3 core/shell nanoparticles, ACS Appl. Mater. Interfaces (2018), https://doi.org/10.1021/acsami.8b12747.
[26] N. Zhang, et al., Silver single-atom catalyst for efficient electrochemical CO2 reduction synthesized from thermal transformation and surface reconstruction, Angew. Chem. Int. Ed. (2021), https://doi.org/10.1002/anie.202014718.
[27] T.J. Wang, et al., Heterostructured Pd/PdO nanowires for selective and efficient CO2 electroreduction to CO, J. Energy Chem. (2022), https://doi.org/10.1016/j.jechem.2022.03.001.
[28] J. Wang, et al., Tailoring the interactions of heterostructured Ni4N/Ni3ZnC0.7 for efficient CO2 electroreduction, J. Energy Chem. (2022), https://doi.org/10.1016/j.jechem.2022.07.037.
[29] S. Ning, et al., Sn-doped CeO2 nanorods as high-performance electrocatalysts for CO2 reduction to formate, ChemElectroChem (2021), https://doi.org/10.1002/celc.202100445.
[30] T. Kou, et al., Amorphous CeO2–Cu heterostructure enhances CO2 electroreduction to multicarbon alcohols, ACS Mater. Lett. (2022), https://doi.org/10.1021/acsmaterialslett.2c00506.
[31] Z. Li, et al., CeO2 nanoparticles with oxygen vacancies decorated N-doped carbon nanorods: a highly efficient catalyst for nitrate electroreduction to ammonia, Nano Res. (2022), https://doi.org/10.1007/s12274-022-4863-8.
[32] X. Ren, et al., Oxygen vacancy enhancing CO2 electrochemical reduction to CO on Ce-doped ZnO catalysts, Surf. Interfaces (2021), https://doi.org/10.1016/j.surfin.2020.100923.
[33] S.S.A. Shah, et al., Metal–organic framework-based electrocatalysts for CO2 reduction, Small Struct. (2022), https://doi.org/10.1002/sstr.202100090.
[34] M. Liu, et al., Enhanced electrocatalytic CO2 reduction via field-induced reagent concentration, Nature (2016), https://doi.org/10.1038/nature19060.
[35] P. Sikam, et al., Effect of 3d-transition metals doped in ZnO monolayers on the CO2 electrochemical reduction to valuable products: first principles study, Appl. Surf. Sci. (2021), https://doi.org/10.1016/j.apsusc.2021.149380.
[36] J. Yin, et al., Customizable CO2 electroreduction to C1 or C2+ products through Cuy/CeO2 interface engineering, ACS Catal. (2022), https://doi.org/10.1021/acscatal.1c04714.
[37] S. Hong, et al., Tuning the C1/C2 selectivity of electrochemical CO2 reduction on Cu-CeO2 nanorods by oxidation state control, Adv. Mater. (2022), https://doi.org/10.1002/adma.202208996.
[38] T. Yang, et al., Interfacial Synergy between the Cu Atomic Layer and CeO2 Promotes CO Electrocoupling to Acetate, ACS Nano (2023), https://doi.org/10.1021/acsnano.3c00817.
[39] X. Zong, et al., Stabilization of oxidation state in ZnO decorated-CeO2 for enhanced formation of CO in CO2 electroreduction, Appl. Surf. Sci. (2023), https://doi.org/10.1016/j.apsusc.2022.155235.
[40] S. Lamaison, et al., Designing a Zn–Ag catalyst matrix and electrolyzer system for CO2 conversion to CO and beyond, Adv. Mater. (2022), https://doi.org/10.1002/adma.202103963.
[41] D. Bhalothia, et al., Reaction pathways for the highly selective and durable electrochemical CO2 to CO conversion on ZnO supported Ag nanoparticles in KCl electrolyte, Appl. Surf. Sci. (2023), https://doi.org/10.1016/j.apsusc.2022.155224.
[42] V.-H. Nguyen, et al., Ag@ZnO porous nanoparticle wrapped by rGO for the effective CO2 electrochemical reduction, Chem. Eng. Sci. (2021), https://doi.org/10.1016/j.ces.2020.116381.
[43] H.Q. Fu, et al., Synergistic Cr2O3@Ag heterostructure enhanced electrocatalytic CO2 reduction to CO, Adv. Mater. (2022), https://doi.org/10.1002/adma.202202854.
[44] I. Stamatelos, et al., Zn-based catalysts for selective and stable electrochemical CO2 reduction at high current densities, ACS Appl. Energy Mater. (2022), https://doi.org/10.1021/acsaem.2c02557.
[45] Y. Zhao, Co-precipitated Ni/Mn shell coated nano Cu-rich core structure: a phase-field study, J. Mater. Res. Technol. (2022), https://doi.org/10.1016/j.jmrt.2022.09.032.
[46] Y. Liu, et al., Interfacial redox reaction-directed synthesis of silver@cerium oxide core–shell nanocomposites as catalysts for rechargeable lithium–air batteries, J. Power Sources (2015), https://doi.org/10.1016/j.jpowsour.2015.03.147.
[47] Z. Li, et al., CuO/ZnO/C electrocatalysts for CO2-to-C2+ products conversion with high yield: On the effect of geometric structure and composition, Appl. Catal. A: Gen. (2020), https://doi.org/10.1016/j.apcata.2020.117829.
[48] W. Ma, et al., Cerium oxide (CeO2-x) nanoparticles with high Ce3+ proportion synthesized by pulsed plasma in liquid, Ceram. Int. (2020), https://doi.org/10.1016/j.ceramint.2020.07.093.
[49] J.P.Y. Tan, et al., Three-dimensional structure of CeO2 nanocrystals, J. Phys. Chem. C. (2011), https://doi.org/10.1021/jp1122097.
[50] B. Ren, et al., Dual-scale integration design of Sn–ZnO catalyst toward efficient and stable CO2 electroreduction, Adv. Mater. (2022), https://doi.org/10.1002/adma.202204637.

[51] P. Li, et al., Tuning the efficiency and product composition for electrocatalytic CO2 reduction to syngas over zinc films by morphology and wettability, Green. Chem. (2022), https://doi.org/10.1039/D1GC04364A.
[52] T. Zhang, et al., Zn electrode with a layer of nanoparticles for selective electroreduction of CO2 to formate in aqueous solutions, J. Mater. Chem. A (2016), https://doi.org/10.1039/C6TA07000K.
[53] J. Zhang, et al., Oxygen vacancies in amorphous InOx nanoribbons enhance CO2 adsorption and activation for CO2 electroreduction, Angew. Chem. Int. Ed. (2019), https://doi.org/10.1002/anie.201900167.
[54] Z. Geng, et al., Oxygen vacancies in ZnO nanosheets enhance CO2 electrochemical reduction to CO, Angew. Chem. Int. Ed. (2018), https://doi.org/10.1002/anie.201711255.
[55] C. Rodwihok, et al., Cerium-oxide-nanoparticle-decorated zinc oxide with enhanced photocatalytic degradation of methyl orange, Appl. Sci. (2020), https://doi.org/10.3390/app10051697.
[56] S. Rajendran, et al., Ce3+-ion-induced visible-light photocatalytic degradation and electrochemical activity of ZnO/CeO2 nanocomposite, Sci. Rep. (2016), https://doi.org/10.1038/srep31641.
[57] K. Sun, et al., Low-operating-temperature NO2 sensor based on a CeO2/ZnO heterojunction, Sensors (2021), https://doi.org/10.3390/s21248269.
[58] S. Rehman, et al., Tuning of ionic mobility to improve the resistive switching behavior of Zn-doped CeO2, Sci. Rep. (2019), https://doi.org/10.1038/s41598-019-55716-4.
[59] Z. Ait Abdelouhab, et al., Structural and morphological characterizations of pure and Ce-doped ZnO nanorods hydrothermally synthesized with different caustic bases, Mater. Sci. -Pol. (2020), https://doi.org/10.2478/msp-2020-0038.
[60] D.L.T. Nguyen, et al., Selective CO2 reduction on zinc electrocatalyst: the effect of zinc oxidation state induced by pretreatment environment, ACS Sustain. Chem. Eng. (2017), https://doi.org/10.1021/acssuschemeng.7b02460.
[61] S. Ali, et al., Bifunctional phosphate-modulated Cu2O/CeO2 redox heterojunction: a promising approach for proficient CO2 reduction, J. Alloy. Compd. (2024), https://doi.org/10.1016/j.jallcom.2023.172766.
[62] J. Ding, et al., Engineering CeO2 configurations to regulate the CuOx dispersion and switch pathways of preferential CO oxidation. Appl. Catal. B: Environ. (2023) https://doi.org/10.1016/j.apcatb.2023.122686.
[63] S.-T. Guo, et al., Stabilizing undercoordinated Zn active sites through confinement in CeO2 nanotubes for efficient electrochemical CO2 reduction, Angew. Chem. (2023), https://doi.org/10.1002/ange.202314099.
[64] Z. Zhang, et al., Two ships in a bottle" design for Zn–Ag–O catalyst enabling selective and long-lasting CO2 electroreduction, J. Am. Chem. Soc. (2021), https://doi.org/10.1021/jacs.0c12418.
[65] K.A. Alim, et al., Micro-Raman investigation of optical phonons in ZnO nanocrystals, J. Appl. Phys. (2005), https://doi.org/10.1063/1.1944222.
[66] G. Jayakumar, et al., A comprehensive investigation on the properties of nanostructured cerium oxide, Opt. Quantum Electron. (2019), https://doi.org/10.1007/s11082-019-2029-z.
[67] B. Chouchene, et al., High performance Ce-doped ZnO nanorods for sunlight-driven photocatalysis, Beilstein J. Nanotechnol. (2016), https://doi.org/10.3762/bjnano.7.125.
[68] C. Schilling, et al., Raman spectra of polycrystalline CeO2: a density functional theory study, J. Phys. Chem. C. (2017), https://doi.org/10.1021/acs.jpcc.7b06643.
[69] T. Rajkumar, et al., Surface engineering of CeO2 catalysts: differences between solid solution based and interfacially designed Ce1−xMxO2 and MO/CeO2 (M = Zn, Mn) in CO2 hydrogenation reaction, Catal. Lett. (2021), https://doi.org/10.1007/s10562-021-03591-y.
[70] Anushree, et al., Synthesis, characterization and catalytic performance of ZnO–CeO2 nanoparticles in wet oxidation of wastewater containing chlorinated compounds, Appl. Nanosci. (2017), https://doi.org/10.1007/s13204-017-0596-5.
[71] S.N.H. Daud, et al., 3D hyperbranched heterostructures of Ag nanocrystals-decorated ZnO nanopillars: controlled growth and characterization of the optical properties, CrystEngComm (2017), https://doi.org/10.1039/C7CE01159H.
[72] S. Gayathri, , 2015, Investigation of physicochemical properties of Ag doped ZnO nanoparticles prepared by chemical route.
[73] F.-C. Liu, et al., Effect of silver dopants on the ZnO thin films prepared by a radio frequency magnetron co-sputtering system, Materials (2017), https://doi.org/10.3390/ma10070797.
[74] G. Shan, et al., Enhanced Raman scattering of ZnO quantum dots on silver colloids, J. Phys. Chem. C. (2007), https://doi.org/10.1021/jp066070v.
[75] R. Zamiri, et al., Far-infrared optical constants of ZnO and ZnO/Ag nanostructures, RSC Adv. (2014), https://doi.org/10.1039/C4RA01563K.
[76] O.M. Lavrynenko, et al., Nanocomposites based on cerium, lanthanum, and titanium oxides doped with silver for biomedical application, Condens. Matter (2022), https://doi.org/10.3390/condmat7030045.
[77] M.V. Grabchenko, et al., Ag/CeO2 composites for catalytic abatement of CO, soot and VOCs, Catalysts (2018), https://doi.org/10.3390/catal8070285.
[78] R.A. Ismail, et al., Preparation and characterization of CeO2 @Ag core/shell nanoparticles by pulsed laser ablation in water, Lasers Manuf. Mater. Process. (2019), https://doi.org/10.1007/s40516-019-00086-y.
[79] Y. Kang, et al., Studies of the catalytic oxidation of CO Over Ag/CeO2 catalyst, Catal. Lett. (2012), https://doi.org/10.1007/s10562-012-0893-2.
[80] M.V. Grabchenko, et al., The role of metal–support interaction in Ag/CeO2 catalysts for CO and soot oxidation, Appl. Catal. B: Environ. (2020), https://doi.org/10.1016/j.apcatb.2019.118148.
[81] Y. Liang, et al., Ag single atoms anchored on CeO2 with interfacial oxygen vacancies for efficient CO2 electroreduction, ACS Appl. Mater. Interfaces (2023), https://doi.org/10.1021/acsami.3c04556.
[82] D. Gao, et al., Enhancing CO2 electroreduction with the metal–oxide interface, J. Am. Chem. Soc. (2017), https://doi.org/10.1021/jacs.7b00102.
[83] S.J. Park, et al., Electrochemical Ce(III)/Ce(IV) redox behavior and Ce oxide nanostructure recovery over thio-terpyridine-functionalized Au/carbon paper electrodes, ACS Appl. Mater. Interfaces (2021), https://doi.org/10.1021/acsami.1c05105.
[84] L. Fang, et al., Operando X-ray absorption spectroscopy study of SnO2 nanoparticles for electrochemical reduction of CO2 to formate, ACS Appl. Mater. Interfaces (2022), https://doi.org/10.1021/acsami.2c17481.